invited

# Modeling of Deep-Submicrometer MOSFETs: Random Impurity Effects, Threshold Voltage Shifts and Gate Capacitance Attenuation

Dragica Vasileska, William J. Gross[1] and David K. Ferry

Department of Electrical Engineering, Arizona State University, Tempe, AZ 85287-5706, USA
Phone: (602) 965-6651, Fax: (602) 965-8058, E-mail: vasilesk@imap2.asu.edu

[1]Intel Corp., Chandler, AZ

## 1. Introduction

With the invention of the transistor in 1947 and the integrated circuit in 1956, the development of large-scale integrated circuits has far surpassed all original dreams. SIA projections show a steady rate of improvement in most key parameters up to the year 2009. At that time the leading edge devices will employ 0.07 µm gate-lengths, which will enable more than 20 million logic gates to be integrated on a single chip. Toshiba, which fabricated $n$-channel MOSFETs with effective gate lengths as short as 27 nm [1], demonstrated that these feature sizes are feasible.

Even though we have not reached any barrier yet, the designers of semiconductor devices are starting to see a variety of undesirable effects that will hinder the performance of deep-submicron devices. Well known problems include:

- the effect of so-called *hot* carriers, and
- *short-channel* effects.

Another potential problem that cannot be controlled in deep-submicrometer devices is due to discrete (atomistic) nature of the impurity atoms. For example, it is well known that in deep-submicrometer devices, to make final threshold voltage adjustments and eliminate the punchthrough effect, ion implantation is used at several steps in the fabrication process. The stochastic nature of ion implantation across the wafer leads to significant deviation in both the number of dopants and the arrangement of these dopant atoms from device to device. As a result, a simplified smooth-background impurity distribution is no longer an acceptable model for the end-of-the-roadmap devices that will have only a few impurity atoms in their active region. Anticipated effects include

- classical statistical effects, such as variation in the threshold voltage or level of current, and
- quantum-mechanical effects, discussed briefly below.

The existence of the surface potential fluctuations in MOS structures was postulated by Nicollian and Goetzberger [2] to explain the departures from the theoretical predictions in conductance versus frequency measurements. Surface potential fluctuations were found to have a large influence on a variety of other device characteristics, such as threshold voltage, transconductance, substrate current and off-state leakage currents [3,4]. Device simulators, such as Drift-Diffusion [5,6] and Hydrodynamic [7], have been extensively used to quantify the variation of the device parameters arising from dopant fluctuations. Even though there is no consensus on the approach that should be pursued to account for these statistical effects, there are indications that besides the Drift-Diffusion (DD) and Hydrodynamic (HD) approaches, particle-based (PB) simulators can also provide useful insight and information in different regimes of device operation.

In this paper, we discuss three different problems related to operation and modeling of the ultra-small devices of the future:

- The influence of the atomistic nature of the impurity atoms on the subthreshold MOSFET characteristics, for which we used our existing three-dimensional (3D) DD simulator.
- Proper inclusion of the electron-electron (*e-e*) and electron-impurity (*e-i*) interactions in a particle-based simulator, to account for the atomistic nature of the impurity atoms and the short-range portions of these two interaction terms.
- The influence of space quantization effect and the depletion of the polysilicon gates on the magnitude of the total gate capacitance $C_{tot}$ and threshold voltage $V_{th}$ in devices with variable oxide thickness.

## 2. Subthreshold MOSFET Characteristics

The geometrical and structural parameters of the device used in this study are the following: $L_G$=0.1 µm, $W_G$=0.05 µm and $t_{ox}$=3 nm. The substrate doping is $N_A$=8×10¹⁷ cm⁻³, whereas the doping of the source and drain regions is $N_D$=10¹⁹ cm⁻³. The length of the discrete doping region equals the gate-length $L_G$ of the device, whereas the depth and the width of the discrete doping region is 58.6 nm and 86.9 nm, respectively. Due to the high doping densities used here, the 3D Poisson and 3D electron current continuity equation are solved assuming Fermi-Dirac (degenerate) statistics with $D_n$ and $\mu_n$ constant ($\mu_n$=300 cm²/V-s). The procedure used for generating the atomistic impurity distribution in the discrete doping region of the device $V_{disc}$ is described in details in [8]. Briefly, we mimic the physical ion-implantation process by drawing a random number $k$ from the Poisson distribution with mean value of the process $a=N_A V_{disc}$. Each of these $k$ impurity atoms is then uniformly distributed within the discrete doping region of the device by

using triplets of independent uniformly distributed random numbers. We use both the nearest-element-cell (NEC) and the cloud-in-cell (CIC) scheme when assigning the charge, i.e. doping density to the node points [9].

A set of 20 transfer characteristics for devices with different number and different distribution of the impurity atoms under the gate is shown in Fig. 1. For comparison, we also show the continuum doping model results and the average current for the discrete model. As discussed in details in [8], the spread of the transfer characteristics along the gate axis is associated to the non-uniformity of the potential barrier, which allows for early turn-on of some parts of the channel. Based on the results shown in Fig. 1, statistical characterization was made for two very important device parameters: threshold voltage $V_{th}$ (equal to the gate voltage $V_G$ for which $I_D=10^{-7}$ A) and turn-off voltage $V_{off}$ (equal to $V_G$ for which $I_D=10^{-10}$ A). We calculated that the standard deviation for both $V_{th}$ and $V_{off}$ is 25.8 mV and 23.8 mV, respectively. In addition to introducing variations to both $V_{th}$ and $V_{off}$, applying atomistic doping distribution in our numerical simulations was found to shift their average values by about -10 mV.
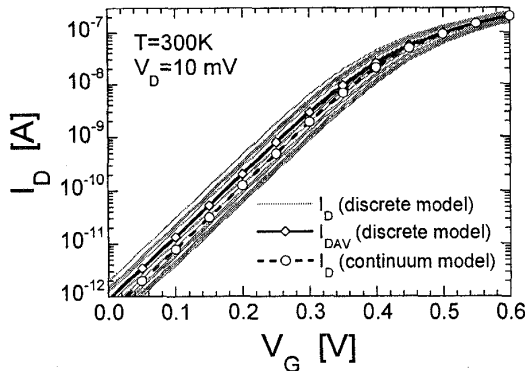


Figure 1. MOSFETs subthreshold transfer characteristics.

We also found a significant correlation between the number of dopants in the part of the discrete doping region that extends down to 7.2 nm from the semiconductor-oxide interface and the magnitude of $V_{th}$ (Fig. 2). The value of the correlation factor dropped to about half this value when taking into account the number of atoms that fall within the total discrete doping region $V_{disc}$. The results for the depth dependence of the correlation factor $r$ shown in Fig. 3, confirm these observations. It is clear that it is not the total number of dopants that fall within the total discrete doping region that affects the magnitude of $V_{th}$, but it is the number of dopant atoms that fall within the first 30-40 nm that are relevant. Hence, analyses that only take into account the number of atoms within the total discrete doping region to describe the fluctuations in the threshold voltage can be very misleading.

It is important to note that identical subthreshold characteristics were obtained when using either the NEC or the CIC scheme for the charge assignment. The subthreshold device characteristics were also not affected with the introduction of discrete doping regions in the source and drain

regions. The dependence of the standard deviation and the average shift of both $V_{th}$ and $V_{off}$ upon the mesh size is currently being investigated.
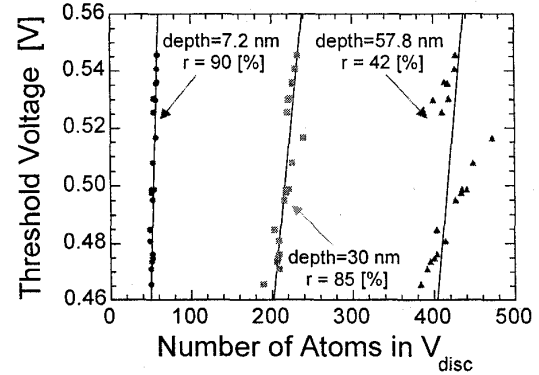


Figure 2. $V_{th}$ versus number of atoms in the discrete doping region. Parameter in this curve is the depth of the discrete doping region taken into consideration. The total depth of $V_{disc}$ is 57.8 nm.
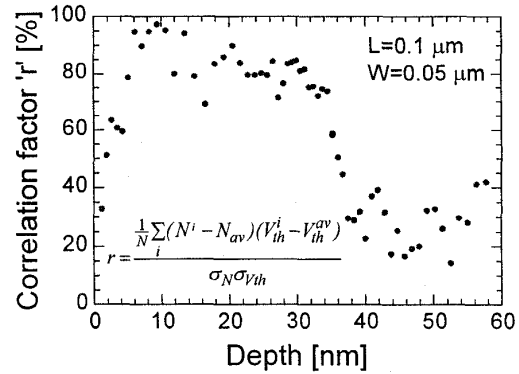


Figure 3. Depth dependence of the correlation factor $r$. $N_i$ is the number of dopants for the $i$-th device that fall within the part of the discrete doping region that extends up to a given depth, whereas $N_{av}$ is the average value of dopant atoms that fall in this region for an ensemble of 20 devices.

## 3. Electron-Electron and Electron-Impurity Interactions

The basic steps involved in a generic particle based simulator are the following [10]:

- *Initialize data* - Set up the geometry of the device, doping profile and discretization scheme.
- *Charge assignment* - The charge of each particle is assigned to the neighboring mesh points.
- *Potential solution* - The 3D Poisson's equation is solved for the electrostatic potential at the mesh points, used to calculate the electric field profile (thus accounting for the long-range portions of the *e-e* and the *e-i* interactions).
- *Flights* - Each particle, treated as individual electron, undergoes the standard MC sequence of scattering and free-flights, subject to the local field determined in the previous step.

The short-range portions of the *e-e* and *e-i* interactions are commonly accounted for by introducing them as additional scattering mechanism in the k-space portion of the Monte Carlo transport kernel. One of the problems with this screened scattering approach is that, unlike the other scattering processes, *e-e* and *e-i* scattering rates need to be re-evaluated frequently during the simulation process to take into account the changes in the distribution function and the screening length. The calculation of the distribution function is highly CPU intensive, and it cannot account for local variations of electron density in real space. Additional problem with this approach is that the localized forces arising from discrete ions can only be determined from the mesh force. If an infinitely small mesh is used, the force calculated from the mesh potentials would be identical to the Coulomb force. But, even a practical solution (spacing in the 2.5 nm range) is very costly in terms of both CPU time and memory.

Herein we propose a new method for calculating the forces on the electrons in a Monte Carlo particle-based simulator. In the following, we will first explain the method for generating the corrected Coulomb force look-up table. Afterwards, we will show that one can successfully use the generated look-up table in calculating the actual force seen by the electrons in a realistic device situation. This approach builds upon the traditional approach of splitting the Coulomb potential into short-range and long-range parts. Here, the grid spacing sets an effective maximum spatial frequency for the potential.

The simulation domain for both experiments was 0.4μm ×0.4μm×0.4μm with 40 grid points along each axis (10 nm uniform spacing in each direction). For generating the corrected Coulomb force look-up table, a single electron (target, or fixed electron) was placed at a known position, while a second electron was swept along the "device" in 0.2 nm increments so that it passed through the first electron. The electron charges were assigned to the nodes using the CIC method. 3D Poisson equation solver, based upon Stone's strongly implicit method, was used to solve for the node potentials. At self-consistency, the field at the position of the swept electron was interpolated from the mesh potential. In a separate experiment, the Coulomb force was calculated using standard Coulomb law. For each electron spacing we tabulated the mesh force $F_{mesh}$, the Coulomb force $F_{coul}$, and the difference between the two $F'=F_{coul}-F_{mesh}$, which we named a corrected Coulomb force. The generated look-up table also provided us important information concerning the determination of the minimum cutoff range for $F'$ based upon the point where $F_{coul}$ and $F_{mesh}$ begin to intersect. The variation of $F_{coul}$, $F_{mesh}$ and $F'$ with the distance between the two electrons taken into account in this experiment is shown in Fig. 4. It is clear that the mesh force and the Coulomb force are identical when the two electrons are separated several mesh points (30-50 nm apart). Within 3-5 mesh points, $F_{mesh}$ starts to deviate from $F_{coul}$. When the electrons are within the same mesh cell, the mesh force approaches zero due to the smoothing of the electron charge when divided amongst the nearest node points. Since the calculated mesh force depends upon the mesh spacing, the corrected

Coulomb force is also a function of the mesh spacing and the position of the electron within the cell. That the electron placement within the node points does indeed affect the mesh force calculation for spacing less than 20 nm is easily seen from the results shown in Fig. 5. Since in this region (Fig. 4) the mesh force contribution is small when compared to the Coulomb force, any error introduced in the mesh force calculation will not influence the total force on the electron.
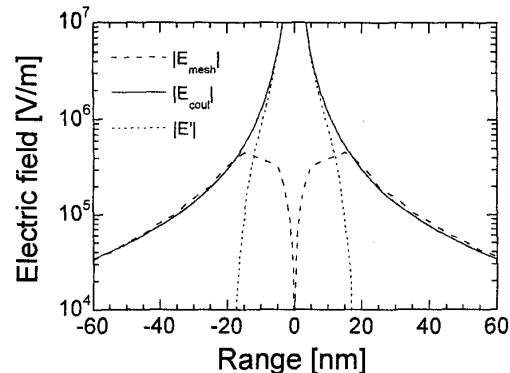


**Figure 4.** Mesh, Coulomb and corrected Coulomb field versus the distance between the two electrons. Note: $F=-eE$.
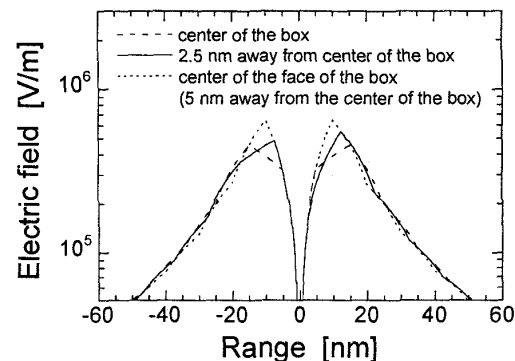


**Figure 5.** Mesh field versus electron separation for different positions of the target (fixed) electron. Curves are offset to allow for proper overlay.

Tabulated values for $F'$, i.e. $E'$, were used in a 3D particle-based simulation of a resistor in place of the molecular dynamic force. The doping of the resistor is about $8\times10^{17}$ cm$^{-3}$, and the applied bias is 0.4 V. An additional electron was swept from the left to the right contact and the $x$-, $y$- and $z$-components of the field were evaluated at each electron's position. The $x$-component of the total field is shown in Fig. 6 (Similar results were obtained for the $y$- and $z$- components). There is very good agreement between the calculated $x$-component of the field and the one obtained by using full molecular dynamics simulations to which a field of $10^6$ V/m was added to account for the applied bias. It is also clear that if one adds the full Coulomb force (calculated with a cut-off range of 20 nm) to the mesh force, the total force on the electrons would be overestimated at distances between our test electron and an electron or an ion larger than several

mesh spacing. On the other hand, if only the Coulomb force is taken into account, in regions where the field arising from the applied bias is important, its contribution would not have been accounted for.
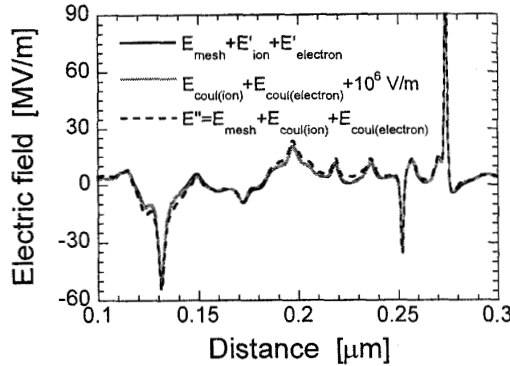


**Figure 6.** Electric field versus distance calculated by our approach and the molecular dynamics approach. Also shown is the field **E"** obtained by adding the Poisson force and the Coulomb force from molecular dynamics simulations with a cutoff range of 20 nm.

## 4. Influence of Space Quantization and Poly-Gate Depletion on $C_{tot}$ and $V_{th}$

Equations describing the C-V curves are usually derived using a number of simplifying assumptions. One modification of these assumptions is the depletion of the polysilicon gates. Other modifications that are significant for sub-10 nm oxide thickness include Fermi-Dirac (F-D) statistics instead of commonly employed Maxwell-Boltzmann (M-B) statistics and space quantization effect in the inversion layer. All of these effects must be considered in deep-submicrometer devices with $t_{ox} < 10$ nm. From the results shown in Fig. 7, obtained with our 1D Schrödinger-Poisson solver, it is obvious that both poly-gate depletion and space-quantization effect will lead to large degradation of $C_{tot}$ and, therefore, to degradation of MOSFET's transconductance.

A shift in the threshold voltage was also observed. Assuming that $V_{th}$ equals the gate voltage $V_G$ for which the sheet inversion charge density is $10^3$ smaller than the depletion charge density, for a MOS capacitor with $t_{ox}=2$ nm, $V_{th}$ is calculated to be 101.5, 195.15, 160.45, 213.75, and 246.35 mV for a device with metal gates and classical charge description, metal gates and quantum-mechanical charge description, poly gates with $N_D=2\times10^{20}$ cm$^{-3}$, $10^{20}$ cm$^{-3}$ and $6\times10^{19}$ cm$^{-3}$ and quantum-mechanical charge description, respectively. Thus, for a device with metal gates, the inclusion of the space-quantization effects leads to threshold voltage shift of about 93.65 mV. If devices with poly-silicon gates with $N_D<10^{20}$ cm$^{-3}$ are considered, the shift in the threshold voltage is even larger.

## 5. Summary

Herein, we presented simulation results for the subthreshold characteristics of *n*-channel MOSFETs with 0.1 μm gate-length and 0.05 μm gate-width obtained with our 3D-DD simulator. We also presented a new method that one can

successfully use in a particle-based simulator to properly account for the short-range portions of the *e-e* and *e-i* interactions without double-counting the long-range portions of these two interaction terms. The correctness of the approach was demonstrated on the example of a resistor. Our existing 1D Schrödinger-Poisson solver, which was recently installed on the Purdue Semiconductor Simulation Hub (www.ecn. purdue.edu/labs/punch), was used to examine the degradation of the total gate capacitance and threshold voltage shifts due to space-quantization effect and the depletion of the poly-silicon gates in devices with ultra-thin oxides.
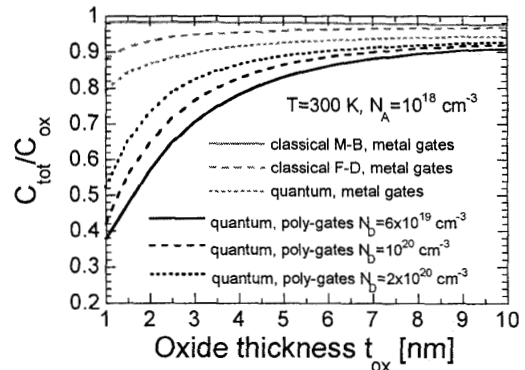


**Figure 7.** Simulated $C_{tot}$ to oxide capacitance $C_{ox}$ for metal/p-substrate and n$^+$-poly/p-substrate MOS capacitors, as a function of the physical oxide thickness $t_{ox}$ and the doping of the polysilicon gates $N_D$ for $V_G$=3 V. The high value for $V_G$ used here may overestimate the severity of the bias dependent attenuation for thinner oxides, but a consistent value for $V_G$ is useful for the purpose of tabulating the simulated results.

## References

1. M. Ono, M. Saito, T. Yoshitomi, C. Fiegna, T. Ohguro and H. Iwai: IEEE Trans. Electron Devices **42** (1995) 1822.
2. E. H. Nicollian and A. Goetzberger: Bell Syst. Techn. J. **46** (1967) 1055.
3. T. Mizuno, J. Okamura and A. Toriumi: IEEE Trans. Electron Devices **41** (1994) 2216.
4. R. Sitte, S. Dimitrijev and H. B. Harrison: IEEE Trans. Electron Devices **41** (1994) 2210.
5. H.-S. Wong and Y. Taur: IEDM Tech. Dig. (1993) 705.
6. P.A. Stolk, F.P. Widdershoven, and D.B.M. Klaassen, IEEE Trans. Electron. Dev. **45** (1998) 1960.
7. J.-R. Zhou and D.K. Ferry: IEEE Comput. Science and Eng. **2** (1995) 30.
8. D. Vasileska, W.J. Gross, V. Kafedziski and D.K. Ferry: VLSI Design, in press.
9. S.E. Laux: IEEE Trans. CAD Integr. Circ. Syst. **15** (1996) 1266.
10. P. Lugli: IEEE Trans. Computer-Aided Design **9** (1990) 1164.